Accurate Simulation of a Shallow-etched Grating Antenna on Silicon-on-insulator for Optical Phased Array Using Finite-difference Time-domain Methods

Dong-Ju Seo and Han-Youl Ryu*

Department of Physics, Inha University, Inchon 22212, Korea

We present simulation methods to accurately determine the transmission efficiency and far-field patterns (FFPs) of a shallow-etched waveguide grating antenna (WGA) formed on a silicon-on-insulator wafer based on the finite-difference time-domain (FDTD) approach. The directionality and the FFP of a WGA with >1-mm in length can be obtained reliably by simulating a truncated WGA structure using a three-dimensional FDTD method and a full-scale WGA using a two-dimensional FDTD with the effective index method. The developed FDTD methods are applied to the simulation of an optical phased array (OPA) composed of a uniformly spaced WGA array, and the steering-angle dependent transmission efficiency and FFPs are obtained in OPA structures having up to 128-channel WGAs.

Keywords : Grating antenna, Optical phased array, Silicon photonics, Numerical modeling
OCIS codes : (050.1755) Computational electromagnetic methods; (130.3120) Integrated optics devices; (230.1950) Diffraction gratings

I. INTRODUCTION

Recently, optical phased arrays (OPAs) based on silicon photonics technology have attracted increasing attention for applications in free-space beam steering of light detection and ranging (LIDAR) systems [1-14]. The OPA offers several advantages such as low cost, reduced size and weight, and increased speed by using the scalability and integrability of silicon photonics. By combining a one-dimensional (1-D) OPA with grating emitters and a tunable laser, beam steering can be achieved in the two-dimensional (2-D) space [3-10]. The emitter elements of OPAs consists of tens or hundreds of waveguide grating antennas (WGAs) arranged either uniformly [3-11] or aperiodically [12-14]. Each WGA is usually formed on the Si waveguide of a silicon-on-insulator (SOI) wafer. The LIDAR applications demand beam steering characteristics such as a wide field of view with high output power in the main lobe and small beam divergence for good spatial resolution. For such purposes, optimum design of an OPA arrangement is required based on reliable simulation methods.

Finite-difference time-domain (FDTD) methods have been frequently employed for designing grating structures on SOI for fiber-grating couplers [15-20] and band-pass filters [21-23]. For such applications, the etch depth of grating structures was typically larger than 50 nm and the length of the grating region was limited to less than ~100 μm. Then, full three-dimensional (3-D) FDTD methods can be applied for simulating such grating devices. However, the dimension of WGAs for the OPA application could be much larger than that of fiber-grating couplers or band-pass filters. To achieve small beam divergence in the longitudinal direction, one needs long WGAs that may be scaled to several millimeters [12, 24]. Therefore, a small grating etch depth relative to the Si waveguide dimension is required to reduce the grating strength, thus increasing the propagation length over the WGA. In Ref. [12], grating etch depth of only ~16 nm was employed in a 400-nm-thick Si rib waveguide. Due to the mm-sized grating length and shallow-etched grating trench, the FDTD simulation of a full-scale WGA has been challenging. In addition, the lateral dimension of an OPA can be larger than 100 μm, which would be

---

*Corresponding author: hanryu@inha.ac.kr, ORCID 0000-0003-4171-4010

too large to be simulated using 3-D FDTD methods. To our knowledge, few attempts have been made to simulate OPA structures using FDTD methods.

In this paper, we present FDTD simulation methods to accurately determine the grating directionality and far-field patterns (FFPs) of a shallow-etched grating antenna formed on a SOI wafer for OPA applications. It will be demonstrated that the directionality and FFP in the lateral direction can be obtained by simulating a truncated WGA of a greatly reduced length using a 3-D FDTD method and the FFP in the longitudinal direction can be obtained by using a 2-D FDTD method with effective refractive index. In this way, simulation time and computational resources can be significantly saved without sacrificing the accuracy of simulation results. The FDTD simulation methods for a shallow-etched grating antenna are applied for simulating OPA structures having up to a 128-channel WGA array to obtain steering-angle dependent FFPs and transmission efficiency.

II. METHODS

Figure 1 shows the schematic of the simulated WGA structure. A Si ridge waveguide with the width, w and the thickness, t_w is formed on a SiO_2 buried oxide (BOX) layer with the thickness t_b. The grating antenna is formed by patterning periodic grooves on the Si waveguide with the etch depth, t_e. The background material outside the WGA and the material of grating grooves are assumed to be air. The total length of the WGA along the z direction is denoted as L_g. An OPA can be formed by 1-D arrangement of WGAs along the x-axis. The beam steering in the phased-array direction (ψ in the xy plane) and the longitudinal direction (θ in the yz plane) is achieved by the phase control between WGAs and the wavelength control, respectively.

For the FDTD simulation of WGA structures, we employed as software, FDTD Solutions by Lumerical Inc. [25]. A perfectly-matched-layer boundary condition was used at all simulation boundaries. A fundamental transverse-electric (TE) mode source was launched as the input mode at the Si waveguide before the grating region. The center wavelength and the full-width at half-maximum (FWHM) of the mode source were set at 1.31 μm and 0.5 μm, respectively. Two power monitors were positioned above the grating patterns in the xz plane and at the end of the grating waveguide in the xy plane to obtain the top transmittance and the forward transmittance, respectively, as shown in Fig. 1(a). The FFPs in both directions (θ and ψ) can be calculated using the field data of the top monitor. The refractive indices of Si and BOX layers were set at 3.45 and 1.45, respectively [26]. Since L_g of actual WGAs comprising an OPA can be extended to several mms, it is challenging to perform 3-D FDTD simulations of a full-structure WGA. Therefore, we performed 3-D FDTD simulations for truncated WGA structures with L_g less than 100 μm and develop the methods to accurately determine the directionality and FFP of actual WGA structures.

In the simulations of this work, the width of the WGA (w) was fixed at 0.4 μm because a narrow emitter is necessary to exhibit wide-angle emission that is required for large steering range in ψ [6, 12]. We considered two kinds of grating antennas (WGA1 and WGA2) with different waveguide thicknesses: t_w of WGA1 and WGA2 was set at 220 and 450 nm, respectively. The grating pitch of WGA1 and WGA2 was respectively chosen to be 560 and 470 nm, corresponding to the emission angle in the θ direction of ~8 degree at 1.31 μm. The duty cycle of gratings was fixed at 50% for both structures. The BOX thickness (t_b) of WGA1 and WGA2 was set at 1300 and 1000 nm, respectively. These values of the BOX thickness were chosen such that a Gaussian-like emission profile can be exhibited in the ψ direction. The etch depth (t_e) of
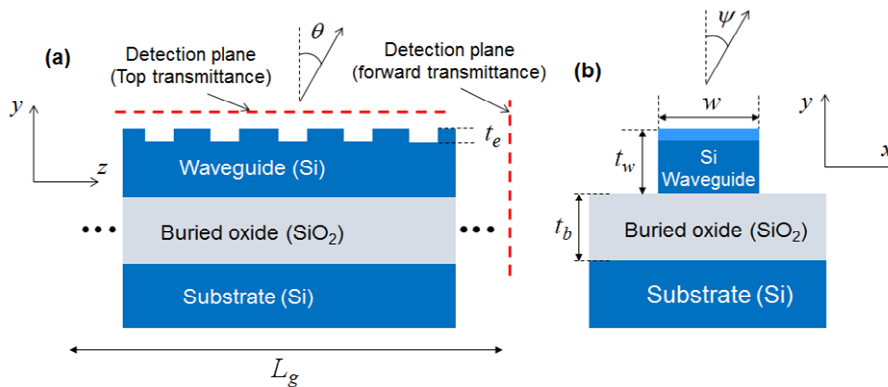

FIG. 1. Schematic of the simulated WGA structure: (a) side view in the yz plane, and (b) front view in the xy plane. A Si waveguide with the width, w and the thickness, t_w is formed on a SiO_2 buried oxide (BOX) layer with the thickness t_b. Periodic grooves with the etch depth, t_e are patterned on the Si waveguide. The beam steering angle in the longitudinal and the lateral direction is denoted as θ in the yz plane and ψ in the xy plane,. The detection planes in the FDTD simulations for the top and forward transmittance are denoted as red dotted lines.

gratings were varied from 10 to 30 nm to obtain narrow beam divergence in the θ direction as mentioned before. Basically, the mesh cells per wavelength were set at 18 in the FDTD simulations of this study, which corresponds to the mesh cell size of ~20 nm in Si layers. In order to represent the shallow-etched grating region appropriately, the mesh cell size of this region was set to be 2 to 5 nm depending on the etch depth. That is, nonuniform mesh structures were employed in the vertical direction of the WGA in our FDTD simulations [25]. We confirmed that our mesh setting gives good convergence of simulation results.

III. SIMULATION RESULTS OF A GRATING ANTENNA

3.1. Grating Directionality

First, the transmittances in the direction above the WGA and in the forward direction are calculated. In the FDTD simulations, the transmittance is determined as the ratio of the power detected in a detection plane to the source power. The detection planes for calculating the top transmittance (T_t) and forward transmittance (T_f) are denoted as dotted lines in Fig. 1. Figure 2(a) plots the top transmittance (T_t) and the forward transmittance (T_f) as L_g varies from 25 to 300 µm for WGA1 ($t_{wg} = 220$ nm) with t_e of 15 nm. As L_g increases, T_t increases and T_f decreases. Since T_f has exponentially decaying dependence on L_g, T_f at distance z is expressed as [15, 27]

$$T_f(z) = T_f(0)\exp(-2\alpha z), \qquad (1)$$

where α is the coupling strength of the grating. α can be obtained from the simulation result of T_f for each L_g. α can

also be determined from the decay of near field profile. Figure 2(b) shows the electric field intensity ($|E|^2$) at the top monitor along the z direction. α is obtained by the linear fit of log($|E|^2$) versus distance as shown in Fig. 2(c). Two methods mentioned above were found to draw the almost identical results on the α value. As t_e increases from 10 to 30 nm, α varies from 1.8 to 15 mm^{-1} for WGA1 and varies from 0.5 to 2.8 mm^{-1} for WGA2, indicating that the coupling strength of the grating increases as the etch depth increases or the waveguide thickness decreases.

Using the α value, T_t at distance x can be obtained as [28]

$$T_t(z) = D[1 - \exp(-2\alpha z)], \qquad (2)$$

where D is the grating directionality which is defined as the ratio between the power diffracted upwards and the input power from the grating. Here, D corresponds to the top transmittance for an infinitely long WGA. Figure 3 shows T_t as a function of L_g for several etch depths of WGA1 and WGA2. Line data were plotted using Eq. (2) with the α value obtained from L_g of 20 µm. Solid dots represent actual full 3-D FDTD simulation results of T_t for L_g from 20 to 500 µm. Two results show good agreements for all cases, implying that the top transmittance and the directionality of a shallow-etched WGA with >1 mm in length can be determined quite accurately by simulating with only a 20-µm-long WGA using a 3-D FDTD method.

The top transmittance becomes saturated at sufficiently long L_g and approaches the D value when the propagating light inside a WGA out-couples to free space almost completely. The grating length where the saturation of the top transmittance occurred increases as α decreases. D of the WGA increases as the etch depth or the Si waveguide
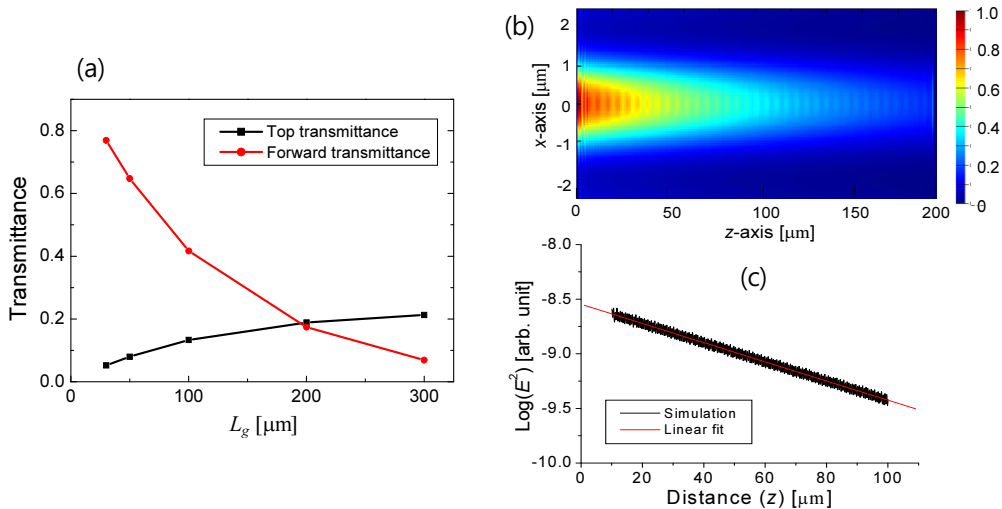

FIG. 2. (a) 3-D FDTD simulation results on top and forward transmittance of the WGA1 as a function of the antenna length (L_g). (b) Electric field intensity ($|E|^2$) distribution at the top monitor along the longitudinal direction (z-direction). (c) Log($|E|^2$) versus distance z. The coupling strength of the grating (α) can be obtained from the linear fit of log($|E|^2$) versus z.
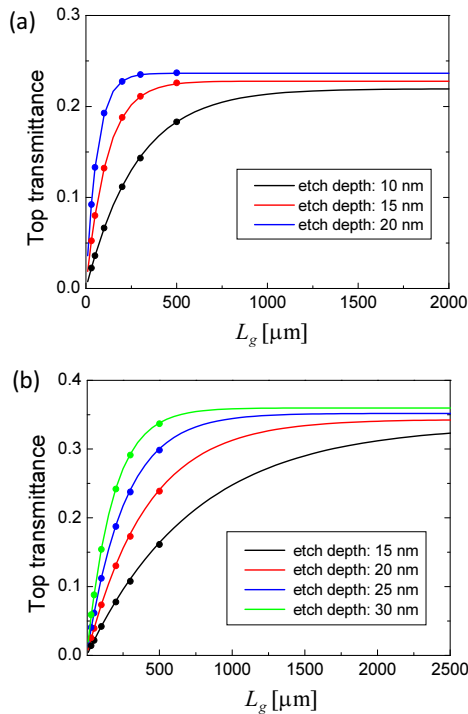
(a)

(b)

FIG. 3. Top transmittance (T_t) is plotted as a function of L_g for (a) WGA1 (t_w = 220 nm) and (b) WGA2 (t_w = 450 nm) for several values of etch depths from 10 to 30 nm. Lines and solid dots represent the results determined by the grating's coupling strength (α) obtained from the 20-µm-long WGA and the full 3-D FDTD simulation for L_g from 20 to 500 µm, respectively.

thickness increases. D of WGA2 can be higher than 0.35 when the etch depth is deeper than 25 nm, whereas that of WGA1 is lower than 0.25 for all values of the etch depth.

3.2. FFP in the Θ Direction

To obtain the FFP in the θ direction correctly, the z-dimension of the top monitor should be sufficiently large (~1 mm). Since the full 3-D FDTD simulation for such a long WGA is impractical, we adopted a 2-D FDTD simulation method with effective refractive index, n_{eff}. In the 2-D FDTD simulation of WGA structures, the x-dimension of the Si waveguide is assumed to be infinite and the refractive index of Si is replaced with n_{eff}. Other parameters such as the grating pitch, the etch depth, the BOX thickness, and L_g remain unchanged. Here, n_{eff} was chosen such that the peak angle in the FFP of the 2-D FDTD simulation could coincide with that of the 3-D FDTD simulation result. n_{eff} was found to be ~3.025 and ~3.098 for WGA1 and WGA2, respectively. Figure 4 shows the FFP in the θ direction for the 2-D FDTD method with effective index and the full 3-D FDTD method when the etch depth is 15 nm and L_g is 100 µm. For both WGA1 and WGA2, the 2-D FDTD method with effective index and the full 3-D FDTD simulation results exhibit the almost identical shape of FFPs. This good correspondence
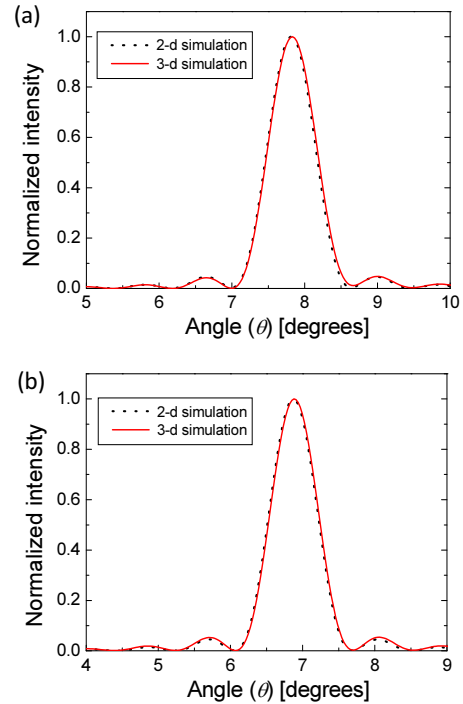

(a)

(b)

FIG. 4. FFP in the θ direction for the 2-D FDTD method with effective index (dotted lines) and the full 3-D FDTD method (solid lines) for (a) WGA1 and (b) WGA2. Here, the etch depth is 15 nm and L_g is 100 µm for both WGA structures.

between the 2-D and the 3-D simulation results has also been found for other values of etch depths and L_g. Consequently, the FWHM as well as the peak angle can be determined with great accuracy by using the 2-D FDTD method with effective refractive index.

Figure 5 shows the 2-D FDTD simulation results of the FWHM in the θ direction for several etch depths of WGA1 and WGA2. The FWHM obtained by the full 3-D FDTD simulation was also plotted as solid dots for L_g up to 500 µm, and reasonably good agreement between the 2-D and the 3-D simulation results are observed. Theoretically, the FWHM in the θ direction for Gaussian beams is given by [3]

$$\Delta\theta = \frac{0.866\lambda_0}{L_g\cos\theta}, \tag{3}$$

where λ_0 is the free-space wavelength. The FWHM given by Eq. (3) is also plotted as dotted lines in Fig. 5.

The simulated FWHM is slightly larger than the theoretical one, which is attributed to the fact that the FFP of the simulated WGAs deviates from the Gaussian beams. As L_g increases, the simulated FWHM begins to saturate and approaches a certain minimum value for a sufficiently long WGA. The saturation of the FWHM occurs when the propagating beam inside a WGA outcouples to free space almost completely as one can see by comparing the results
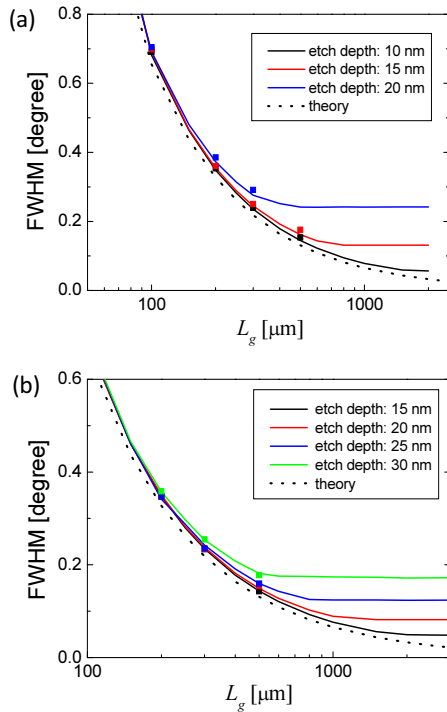
FIG. 5. FWHM in the θ direction for (a) WGA1 and (b) WGA2. Lines and solid dots represent the results obtained by the 2-D FDTD method with effective index for several values of the etch depth and the 3-D FDTD method, respectively. Theoretical FWHM values are also plotted as dotted lines.
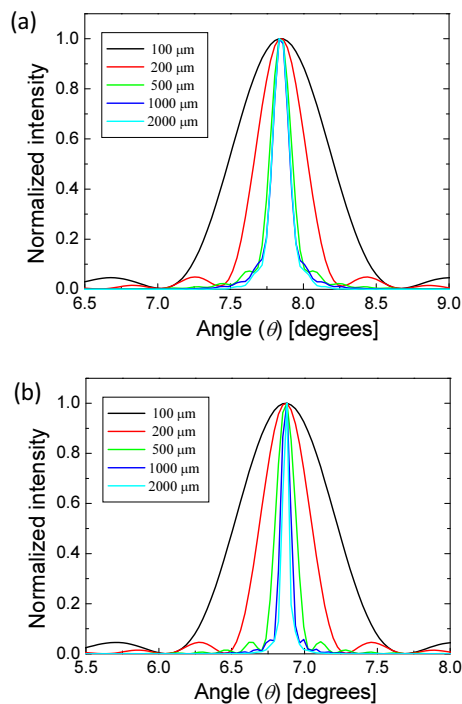
of Figs. 3 and 5. The minimum $\Delta\theta$ decreases as the etch depth decreases or the waveguide thickness increases. To achieve $\Delta\theta$ less than 0.1°, the grating etch depth should be as shallow as 10 nm for WGA1 and 20 nm for WGA2. If the grating etch depth needs to be deeper than 15 nm due to the limitation of fabrication, the divergence angle of less than 0.1° is difficult to be achieved in a thin Si waveguide of the thickness 220 nm.

Figure 6 depicts normalized FFPs in the θ direction simulated by the 2-D FDTD method with effective refractive index for WGA1 and WGA2. The etch depth is 15 nm for both WGAs. As L_g increases, the beam divergence becomes narrower and begins to saturate for sufficiently long L_g. The minimum FWHM is ~0.12° and ~0.05° for WGA1 and WGA2, respectively. The required L_g for obtaining such minimum FWHM values is ~800 μm for WGA1 and ~2000 μm for WGA2.

3.3. FFP in the ψ Direction

We employed the 3-D FDTD method for simulating FFPs in the ψ direction. Figure 7 shows the FFP in the ψ direction for L_g values from 5 to 100 μm. Here, the grating etch depth was fixed at 15 nm for both WGA1 and WGA2. For both WGA structures, little difference in FFP is observed when L_g is larger than 10 μm. When L_g is 5 μm, FFP deviates slightly from other values of L_g. This result implies that FFP in the ψ direction can be determined

FIG. 6. Normalized FFPs in the θ direction simulated by the 2-D FDTD method with effective refractive index for (a) WGA1 and (b) WGA2 as L_g is varied from 100 to 2000 μm. The etch depth is fixed at 15 nm for both WGA structures.
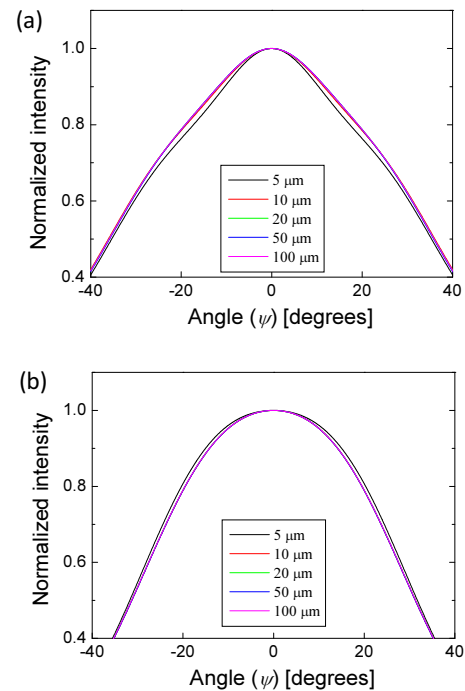

FIG. 7. 3-D FDTD simulation results of FFPs in the ψ direction for (a) WGA1 and (b) WGA2 as L_g is varied from 5 to 100 μm. Here, the grating etch depth is fixed at 15 nm for both WGA structures. Little difference in FFP is observed when L_g is equal to or larger than 10 μm for both structures.

quite accurately using 3-D FDTD simulation with L_g equal to or larger than 10 μm, which does not require great computational resources. In addition, it was found that the FFP in the ψ direction did not change greatly with the variation of the etch depth from 10 to 30 nm.

Figure 8 shows the FFP in the ψ direction for several values of the BOX layer thickness. Here, L_g was fixed at 20 μm. The FFP is strongly influenced by the thickness of the BOX layer because of the interference between the light diffracted at grating patterns, the light reflected at the interface of the Si waveguide and BOX, and the light reflected at the interface of the BOX and Si substrate. This interference effect greatly modifies the FFP as well as the top transmittance. As mentioned in Section II, the BOX layer thickness of WGA1 and WGA2 was respectively chosen to be 1300 and 1000 nm, which resulted in the Gaussian-like FFP as shown in Fig. 8. When the BOX thickness is 1200 nm for WGA1 and 900 nm for WGA2, strong constructive interference in the vertical direction is observed. On the contrary, when the BOX thickness is 1400 nm for WGA1 and 1100 nm WGA2, double lobes are observed as a result of the constructive interference around 30°. Since the ψ-direction FFP of the WGA acts as the envelop function in the FFP of an OPA [3, 12], choosing the proper BOX layer thickness is important to achieve desirable beam steering characteristics in the OPA application.
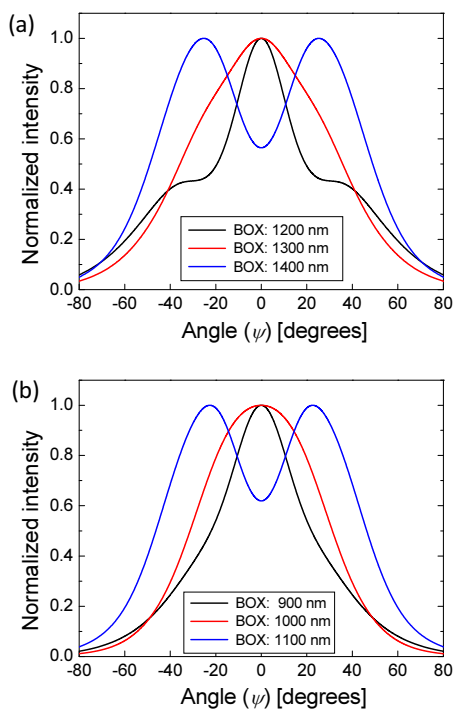
IV. SIMULATION RESULTS OF OPA

In this section, we apply the FDTD methods in Section 3 for simulating the top transmittance and FFP of OPA structures. Figure 9 schematically shows the top-view of a simulated OPA structure that consists of a uniformly spaced 1-D WGA array. Here, the number of WGAs and the spacing between WGAs are denoted as N and d, respectively. As the WGA element comprising the OPA, we adopt WGA2 with the BOX thickness 1000 nm and the etch depth 20 nm, which showed relatively high directionality of ~0.34 and the low minimum FWHM of <0.1° in the θ direction. An OPA with uniformly spaced WGAs generates higher-order grating lobes in addition to the main lobe. The angles of grating lobes are given by [13]

$$\sin \psi_m = \frac{m\lambda}{d} + \sin \psi_0, \qquad (4)$$

where d is the spacing between WGAs, m is the order of the grating lobe, Ψ_m is the angle of the m-th order grating lobe, and Ψ_0 is the angle of the main lobe. As d increases, the angle between the main lobe and the 1-st order grating lobe decreases, limiting the beam steering range in the ψ direction. To cover the beam steering range approaching ±90°, d should be as small as half wavelength, ~0.65 μm. However, this sub-micron pitch could result in significant crosstalk with adjacent WGAs and large beam divergence angle. According to the result of Ref. 13, the crosstalk of our WGA structure would be negligible if d is 1.2 μm or larger. Therefore, we set d to be 1.2 μm for the simulation of the OPA. In this choice of d, the steering range is limited to ~±33°. For the 3-D FDTD simulation of OPAs, L_g is set at 20 μm, which has shown good accuracy in the result of top transmittance and FFP in the ψ direction as

FIG. 8. Normalized FFPs in the ψ direction for (a) WGA1 and (b) WGA2. Here, the BOX layer thickness is varied from 1200 to 1400 nm for WGA1 and varied from 900 to 1100 nm for WGA2. L_g is fixed at 20 μm for both WGA structures.
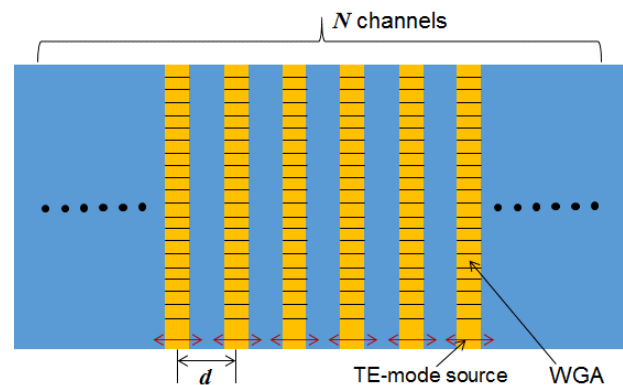

FIG. 9. The top-view of the simulated OPA structure is schematically shown. The OPA consists of uniformly spaced identical WGAs. Here, the number of WGAs and the spacing between WGAs are denoted as N and d, respectively. The TE-mode sources are launched at the input waveguide of WGAs.

demonstrated in Section 3. With this L_g value, OPAs having more than 100 channels can be simulated with 3-D FDTD methods using moderate computational resources.

Figure 10(a) shows the main-lobe FFP in the ψ direction for 16, 32, 64, and 128 channel OPAs when the center angle of the main lobe is 0°. The FFP intensity is normalized to the peak intensity of the 16-channel OPA. As the number of OPA channels increases the peak intensity increases and the FWHM becomes narrower because the total length of the OPA in the x-direction increases with increasing number of channels. As shown in Fig. 10(b), the FWHM decreases from 3.2° to 0.5° as the number of channels increases from 16 to 128. Similarly to the FWHM in the θ-direction
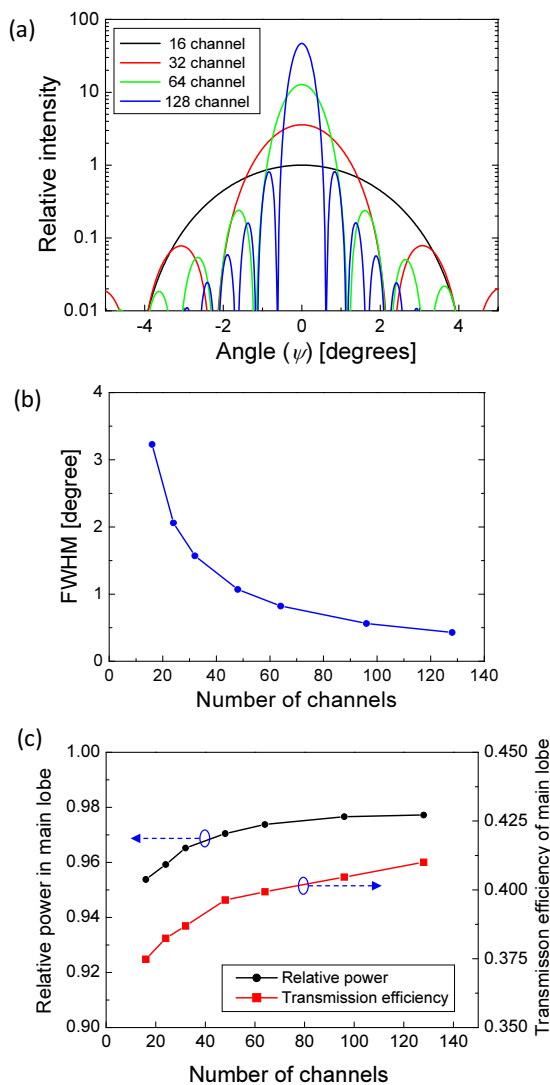
in Eq. (3), the FWHM in the ψ-direction is given by

$$\Delta \psi = \frac{0.866\lambda_0}{Nd\cos\theta} . \qquad (5)$$

The simulated FWHM in Fig. 10(b) agrees well with the theoretical expression in Eq. (5).

Figure 10(c) plots the relative power and transmission efficiency of the main lobe as a function of the number of OPA channels. Here, the relative power in the main lobe is obtained by calculating the power in the main lobe divided by the total radiated power in the upward direction. The transmission efficiency of the main lobe is defined as the ratio of the power in the main lobe to the source power of the OPA input, which is calculated by multiplying the directionality of the OPA and the relative power in the main lobe. The directionality of the OPA can be obtained from Eqs. (1) and (2) using the calculated top transmittance and the α value. The relative power of the 16-channel OPA is as high as 0.95 and increases slowly as the number of channels increases, implying that most of the radiated power is concentrated in the main lobe. The transmission efficiency of the main lobe also increases with increasing number of the OPA. However, the transmission efficiency is limited to be only ~0.4 because more than half of the
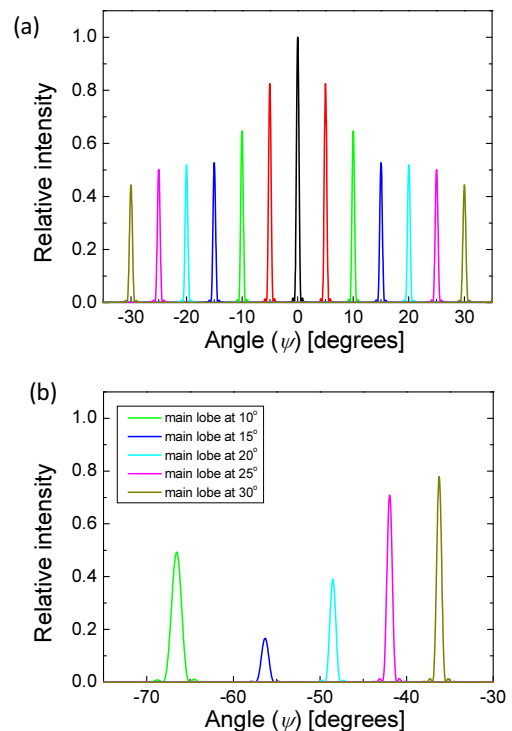

FIG. 10. (a) FFP in the ψ direction around 0° for 16, 32, 64, and 128 channel OPAs when the center of the main lobe is 0°. The FFP intensity is normalized to the peak intensity of the 16-channel OPA. (b) FWHM of the main lobe in the ψ direction as a function of the number of OPA channels. (c) Relative power and transmission efficiency of the main lobe as a function of the number of OPA channels.

FIG. 11. (a) Relative FFP intensity of the main lobe in the ψ direction from -30° to 30° with 5° step for the 128-channel OPA. (b) Relative FFP intensity of the 1-st order grating lobe as the main lobe moves from 0 to 30°. The intensity is normalized to the peak intensity of the main lobe at 0°.

input power seems to be out-coupled in the direction of the BOX and Si substrate.

The beam steering characteristics of the 128-channel OPA are simulated varying the relative phase between adjacent WGAs. Figure 11(a) shows the relative FFP intensity of the main lobe from -30° to 30° with 5° step for the 128-channel OPA. The intensity was normalized to the peak intensity of the main lobe at 0°. The envelope of the relative FFP intensity roughly follows the FFP of a single WGA in Fig. 8(b) for the BOX thickness of 1000 nm. Although the direct interaction between WGAs of the OPA can be negligible, the adjacent WGAs can interact indirectly via the reflected light at the interface of the BOX and Si substrate, which results in the slight difference in the FFP envelope between the single WGA and the OPA. Figure 11(b) shows relative FFP intensity of the 1-st order grating lobe as the main lobe moves from 0 to 30°. No higher-order grating lobes are observed when the main lobe exists at 0 and 5°. However, the 1st-order grating lobe begins to appear for the main lobe angle greater than or equal to 10°.

In Fig. 12(a), the FWHM is plotted as a function of the steering angle in the ψ direction. The FWHM increases as the angle ψ increases. The theoretical FWHM in Eq. (5) is also plotted as dotted lines for comparison. The simulated FWHM is slightly larger than the theoretical one because Eq. (5) corresponds to the minimum FWHM for a Gaussian beam profile. The FWHM is larger than 0.4°, which may not be sufficiently narrow to exhibit good spatial resolution. To decrease the FWHM without sacrificing the steering range, an even larger number of OPA channels is required [9, 13].

Figure 12(b) plots the relative power and the transmission efficiency of the main lobe as a function of the steering angle in the ψ direction. As the angle increases, the relative power and transmission efficiency decrease. In particular, they decrease abruptly when ψ is larger than 5° because an adjacent grating lobe begins to enter the field of view for the main lobe angle larger than 5°. In Fig. 11(b), it was observed that the peak intensity of the 1-st order grating lobe for the main lobe angle of 10° was higher than that for the main lobe angle of 15°, which resulted in the lower relative power and transmission efficiency for the main lobe angle at 10° as compared to the case for the main lobe angle at 15°.

Although the transmission efficiency of the main lobe is >0.4 when ψ is 0° and 5°, it decreases below 0.15 when ψ is 10° or more due to the appearance of the adjacent grating lobe. In order to increase the transmission efficiency of the main lobe, the optimization of the basic WGA structure as well as the optimization an aperiodic WGA array can exhibit only a main lobe without higher-order grating lobes, the optimization of the aperiodic array is expected to lead to increased transmission efficiency by minimizing background side-lobe noise [12, 13]. For these purposes, the FDTD simulation methods presented in this paper can be advantageously employed.

V. CONCLUSION

In this work, we presented FDTD-based numerical methods to accurately determine the coupling efficiency and FFPs of a shallow-etched WGA for OPA applications. The directionality and FFP in the lateral direction (ψ direction) of a WGA with >1-mm in length could be determined by simulating only a ~20 μm-long WGA with a 3-D FDTD method. The FFP in the longitudinal direction (θ direction) was found to be obtained with great accuracy using a 2-D FDTD method with effective refractive index. A relatively high directionality of ~0.35 and a narrow beam divergence of <0.1° was obtained from a WGA with a 450-nm-thick Si waveguide and ~20-nm etch depth. The developed FDTD simulation methods were applied for simulating the beam characteristics of OPAs composed of a uniformly spaced 1-D WGA array. The FFP in the ψ direction and the transmission efficiency of the main beam were obtained in the OPA structure having up to 128-channel WGAs using 3-D FDTD simulations. The simulation methods presented in this work are expected to be advantageously employed for fast design of the OPA structures with optimum beam steering characteristics for LIDAR applications.
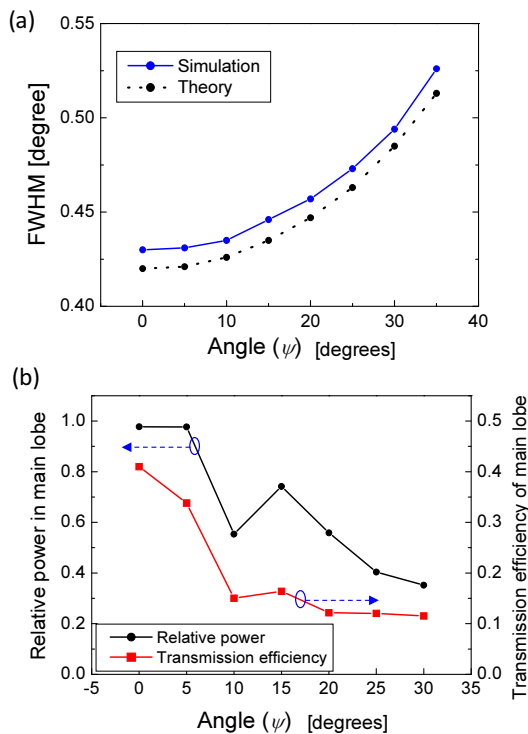

FIG. 12. (a) FWHM is plotted as a function of the steering angle in the ψ direction. Solid and dotted line represents the FDTD simulation result and the theoretical one, respectively. (b) Relative power and transmission efficiency of the main lobe as a function of the steering angle in the ψ direction.

ACKNOWLEDGMENT

REFERENCES

1. M. J. R. Heck, "Highly integrated optical phased arrays: photonic integrated circuits for optical beam shaping and beam steering," Nanophotonics **6**, 93-107 (2017).

2. J. Sun, E. Timurdogan, A. Yaacobi, E. S. Hosseini, and M. R. Watts, "Large-scale nanophotonic phased array," Nature **493**, 195-199 (2013).

3. K. V. Acoleyen, W. Bogaerts, J. Jágerská, N. L. Thomas, R. Houdré, and R. Baets, "Off-chip beam steering with a one-dimensional optical phased array on silicon-on-insulator," Opt. Lett. **34**, 1477-1479 (2009).

4. J. K. Doylend, M. J. R. Heck, J. T. Bovington, J. D. Peters, L. A. Coldren, and J. E. Bowers, "Two-dimensional free-space beam steering with an optical phased array on silicon-on-insulator," Opt. Express **19**, 21595-21604 (2011).

5. D. Kwong, A. Hosseini, J. Covey, Y. Zhang, X. Xu, H. Subbaraman, and R. T. Chen, "On-chip silicon optical phased array for two-dimensional beam steering," Opt. Lett. **39**, 941-944 (2014).

6. A. Yaacobi, J. Sun, M. Moresco, G. Leake, D. Coolbaugh, and M. R. Watts, "Integrated phased array for wide-angle beam steering," Opt. Lett. **39**, 4575-4578 (2014).

7. J. C. Hulme, J. K. Doylend, M. J. R. Heck, J. D. Peters, M. L. Davenport, J. T. Bovington, L. A. Coldren, and J. E. Bowers, "Fully integrated hybrid silicon two dimensional beam scanner," Opt. Express **23**, 5861-5874 (2015).

8. C. V. Poulton, A. Yaacobi, D. B. Cole, M. J. Byrd, M. Raval, D. Vermeulen, and M. R. Watts, "Coherent solid-state LIDAR with silicon photonic optical phased arrays," Opt. Lett. **42**, 4091-4094 (2017).

9. H. Abe, M. Takeuchi, G. Takeuchi, H. Ito, T. Yokokawa, K. Kondo, Y. Furukado, and T. Baba, "Two-dimensional beam-steering device using a doubly periodic Si photonic-crystal waveguide," Opt. Express **26**, 9389-9397 (2018).

10. W. Xie, T. Komljenovic, J. Huang, M. Tran, M. Davenport, A. Torres, P. Pintus, and J. Bowers, "Heterogeneous silicon photonics sensing for autonomous cars," Opt. Express **27**, 3642-3663 (2019).

11. S. H. Kim, J. B. You, Y. G. Ha, G. Kang, D. S. Lee, H. Yoon, D. E. Yoo, D. W. Lee, K. Yu, C. H. Youn, and H. H. Park, "Thermo-optic control of the longitudinal radiation angle in a silicon-based optical phased array," Opt. Lett. **44**, 411-414 (2019).

12. D. N. Hutchison, J. Sun, J. K. Doylend, R. Kumar, J. Heck, W. Kim, C. T. Phare, A. Freshali, and H. Rong, "High-resolution aliasing-free optical beam steering," Optica **3**, 887-890 (2016).

13. T. Komljenovic, R. Helkey, L. Coldren, and J. E. Bowers, "Sparse aperiodic arrays for optical beam forming and LIDAR," Opt. Express **25**, 2511-2528 (2017).

14. D. Zhang, F. Zhang, and S. Pan, "Grating-lobe-suppressed optical phased array with optimized element distribution," Opt. Commun. **419**, 47-52 (2018).

15. D. Taillaert, P. Bienstman, and R. Baets, "Compact efficient broadband grating coupler for silicon-on-insulator wave-guides," Opt. Lett. **29**, 2749-2751 (2004).

16. Y. Wang, W. Shi, X. Wang, Z. Lu, M. Caverley, R. Bojko, L. Chrostowski, and N. A. F. Jaeger, "Design of broadband subwavelength grating couplers with low back reflection," Opt. Lett. **40**, 4647-4650 (2015).

17. M. H. Lee, J. Y. Jo, D. W. Kim, Y. Kim, and K. H. Kim, "Comparative study of uniform and nonuniform grating couplers for optimized fiber coupling to silicon waveguides," J. Opt. Soc. Korea **20**, 291-299 (2016).

18. T. Sharma, H. Kwon, J. Park, S. Han, G. Son, Y. Jung, and K. Yu, "Coupling performance enhancement using SOI grating coupler design," Opt. Commun. **427**, 452-456 (2018).

19. Y. S. Hong, C. H. Cho, and H. K. Sung, "Theoretical analysis of simultaneously improving the light coupling efficiency and bandwidth between two separated grating couplers using integrated distributed Bragg reflectors," J. Korean Phys. Soc. **71**, 647-651 (2017).

20. M. Zhang, H. Liu, B. Wang, G. Li, and L. Zhang, "Efficient grating couplers for space division multiplexing applications," IEEE J. Sel. Top. Quantum Electron. **24**, 8200605 (2018).

21. H. Qiu, G. Jiang, T. Hu, H. Shao, P. Yu, J. Yang, and X. Jiang, "FSR-free add-drop filter based on silicon grating-assisted contradirectional couplers," Opt. Lett. **38**, 1-3 (2013).

22. B. Naghdi and L. R. Chen, "Silicon photonic contra-directional couplers using subwavelength grating waveguides," Opt. Express **24**, 23429-23438 (2016).

23. B. Liu, Y. Zhang, Y. He, X. Jiang, J. Peng, C. Qiu, and Y. Su, "Silicon photonic bandpass filter based on apodized subwavelength grating with high suppression ratio and short coupling length," Opt. Express **25**, 11359-11364 (2017).

24. M. Raval, C. V. Poulton, and M. R. Watts, "Unidirectional waveguide grating antennas with uniform emission for optical phased arrays," Opt. Lett. **42**, 2563-2566 (2017).

25. FDTD Solutions, *Lumerical Inc.*, Available: http://www.lumerical.com/tcad-products/fdtd/ (2019).

26. E. D. Palik, *Handbook of Optical Constants of Solids III,* (Academic Press, Cambridge, MA, USA, 1998).

27. M. Zadka, Y. C. Chang, A. Mohanty, C. T. Phare, S. P. Roberts, and M. Lipson, "On-chip platform for a phased array with minimal beam divergence and wide field-of-view," Opt. Express **26**, 2528-2534 (2018).

28. K. Han, V. Yurlov, and N. E. Yu, "Highly directional waveguide grating antenna for optical phased array," Curr. Appl. Phys. **18**, 824-828 (2018).